

Rapid Assembly of Small Materials Building Blocks (Voxels) into Large Functional 3D Metamaterials

Vincent Hahn,* Pascal Kiefer, Tobias Frenzel, Jingyuan Qu, Eva Blasco, Christopher Barner-Kowollik, and Martin Wegener

Herein, various 3D additive manufacturing approaches are reviewed in terms of two important figures of merit: maximum voxel printing rate and minimum voxel size. Voxel sizes from several 100 μm down to the 100 nm scale are covered. Original results on multifocus two-photon printing at around voxel printing rates of 10^7 voxels s^{-1} are presented in this context, which significantly surpass previous best values. These advances are illustrated by and applied to the making of microstructured 3D (chiral) mechanical metamaterials that are composed of more than one-hundred-thousand unit cells in three dimensions. Previous best values for unit cells of similar complexity are smaller by two orders of magnitude.

1. Introduction

3D additive manufacturing is a megatrend, with numerous applications in mechanics, optics, and the life sciences. Its spirit is to assemble small material building blocks referred to as 3D volume elements or voxels—the 3D counterpart of pixels (2D picture elements)—into large and complex 3D functional architectures. This allows the making of 3D architectures that seemed difficult if not impossible to make previously. Furthermore, 3D additive manufacturing provides great flexibility. It is

no more an effort to 3D print a different architecture each time than it is to make the same structure repeatedly. This flexibility is obviously only meaningful if the overall duration of the 3D manufacturing process is acceptable for the user.

Therefore, the first important figure of merit (FOM) is the rate by which voxels can be 3D printed. This rate can be seen as the speed by which digital information in units of bits is converted into hardware. The second important FOM of 3D additive manufacturing is the minimum accessible voxel size. Whenever the voxel is not spherical, for simplicity, we define

the voxel size by the average of lateral and axial voxel diameter. Many applications, for example in optics, require nanometer roughness, nanometer voxels, and even nanometer resolution. Other applications, for example in biological cell culture, can be realized with micrometer-sized voxels. The product of the individual voxel volume and the 3D voxel printing rate equals the rate of 3D printed volume. A fully scalable technology would need to keep the volume printing rate constant when reducing the voxel size. For example, when reducing the voxel size by a factor of ten, hence reducing the voxel volume by factor $10^3 = 1000$, the voxel printing rate would need to be increased 1000-fold. Such fully scalable 3D additive manufacturing technology is presently elusive. A third and somewhat independent important figure of merit is the number of dissimilar materials that can be 3D printed by any one approach.^[1]

The purpose of this progress report is twofold. First, we review various conceptually different 3D additive manufacturing approaches in terms of the first two important FOM, namely, the voxel printing rate and the voxel size. Our way of representing the available data sheds a fair and a rather different light on the field than previous work (Figure 4 in ref. [2]), in which the voxel printing rate does not even appear. We briefly summarize the operation principle in each case. Second, we present our own original results using multifocus two-photon 3D laser nanoprinting and rapid scanning by motorized mirrors. These results are at the state-of-the-art concerning voxel size and they surpass the state-of-the-art regarding voxel printing rate by more than a factor of 30. As an example that has lately been established and that has attracted interest,^[3] we manufacture microstructured 3D micropolar chiral and achiral mechanical metamaterials. These artificial materials can be applied, for example, to convert an axial motion of a piezoelectric actuator into a twist motion. In about two days printing time (i.e., total time including all settling times etc.), we achieve

V. Hahn, P. Kiefer, T. Frenzel, Dr. J. Qu, Prof. M. Wegener
Institute of Applied Physics (APH)
Karlsruhe Institute of Technology (KIT)
76128 Karlsruhe, Germany
E-mail: v.hahn@kit.edu

V. Hahn, Dr. J. Qu, Dr. E. Blasco, Prof. M. Wegener
Institute of Nanotechnology (INT)
Karlsruhe Institute of Technology (KIT)
76128 Karlsruhe, Germany

Dr. E. Blasco, Prof. C. Barner-Kowollik
Macromolecular Architectures
Institute for Technical Chemistry and Polymer Chemistry (ITCP)
Karlsruhe Institute of Technology (KIT)
76128 Karlsruhe, Germany

Prof. C. Barner-Kowollik
School of Chemistry, Physics and Mechanical Engineering
Queensland University of Technology (QUT)
2 George Street, Brisbane, QLD 4000, Australia

 The ORCID identification number(s) for the author(s) of this article can be found under <https://doi.org/10.1002/adfm.201907795>.

© 2020 The Authors. Published by WILEY-VCH Verlag GmbH & Co. KGaA, Weinheim. This is an open access article under the terms of the Creative Commons Attribution License, which permits use, distribution and reproduction in any medium, provided the original work is properly cited.

DOI: 10.1002/adfm.201907795

more than one hundred thousand 3D unit cells, composed of about three hundred billion voxels. Previous largest values were around five hundred 3D unit cells, printed with commercial technology using only one focus in about one day^[3] (again total time)—which is more than one hundred times slower. These results can additionally be compared to three galleries of 3D metamaterial architectures made by various 3D manufacturing approaches and summarized in a recent comprehensive review article.^[4]

2. State of the Art and Figures of Merit

Figure 1 summarizes various 3D additive manufacturing approaches in terms of two FOM: The upper horizontal logarithmic axis spans five orders of magnitude in voxel size from 1 mm (left) down to 10 nm (right). The lower horizontal scale is the corresponding inverse voxel size. Loosely speaking, resolution or fineness increases toward the right-hand side. The vertical logarithmic scale covers nine orders of magnitude in voxel printing rate from 10^{-1} voxels s^{-1} (bottom) to 10^8 voxels s^{-1} (top). The gray parallel diagonal straight lines with a slope of three in this double-logarithmic representation are lines of constant 3D volume printing rate (see Section 1). An ideal scalable technology moves along these diagonals when changing the voxel size and is located in the upper right-hand side corner of Figure 1.

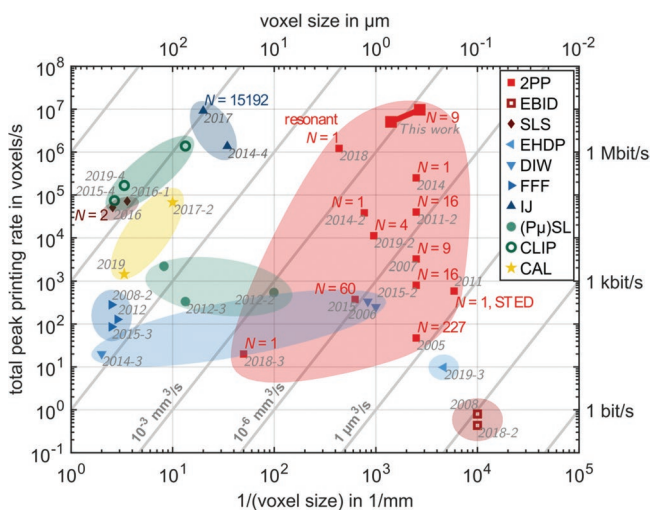


Figure 1. Different 3D additive manufacturing approaches (different symbols, see legend) plotted versus inverse voxel size (lower logarithmic horizontal scale) and total peak printing rate (left logarithmic vertical scale). The upper horizontal scale provides the voxel size itself, and the right vertical scale the bit rate. Electron-beam-induced deposition (EBID, red open squares), selective laser sintering (SLS, dark-red diamonds), electrohydrodynamic (redox) printing (EHDP, light-blue left-pointing triangles), direct ink writing (DIW, light-blue downward-pointing triangles), fused filament fabrication (FFF, blue right-pointing triangles), inkjet 3D printing (IJ, dark-blue upward-pointing triangles), projection microstereolithography (PμSL, light-green discs), continuous liquid interphase printing (CLIP, dark-green circles), computed axial lithography (CAL, yellow stars), and two-photon printing (2PP, red squares). The references underlying the depicted data points are given in the main text. The result of the present work at around a best-case voxel size of 400 nm and a printing speed of 0.9×10^7 voxels s^{-1} is emphasized by the large red square labeled “This work.” The second connected point shows the same result, however, using an averaged voxel size within the 3×3 array of laser foci.



Vincent Hahn studied physics at the Karlsruhe Institute of Technology (KIT) in Germany and obtained his master's degree in 2016. In 2014, he did a research visit at the University of Illinois at Urbana-Champaign (USA). Before starting his Ph.D. in 2016, he worked for Trumpf Photonics Inc. in Cranbury, New Jersey (USA). During his Ph.D. within Martin Wegener's group at KIT, his research focus lies on parallelization methods for 3D microprinting.



Pascal Kiefer is a Ph.D. student in physics under the supervision of Prof. Martin Wegener. His research interests lie in the development of sensitive photoresist as well as parallelization methods for 3D microprinting. He is a physicist by training and obtained his master's degree in 2019 from Karlsruhe Institute of Technology (KIT) in Karlsruhe, Germany. From 2012–2018, he worked at the Fraunhofer Institute of Optronics, System Technologies and Image Exploitation (IOSB) in Ettlingen, Germany. In 2019, he did a research internship at the Institute for Integrated Cell-Material Sciences (iCeMS) in Kyoto, Japan.



Martin Wegener completed his diploma and Ph.D. in physics at Johann Wolfgang Goethe-Universität Frankfurt (Germany) in 1986 and 1987, respectively. He then spent two years as a postdoc at AT&T Bell Laboratories in Holmdel (USA). From 1990–1995, he was a professor at Universität Dortmund (Germany). Since 1995, he has been a professor at the Institute of Applied Physics of Karlsruhe Institute of Technology (KIT). Since 2001, he has been additionally department head at the Institute of Nanotechnology (INT) of KIT and since 2016, he has been a director at INT. Since 2018, he has been a spokesperson of the Cluster of Excellence 3D Matter Made to Order.

Some of the data points in Figure 1 correspond to sequential techniques, which are often prejudiced believed to be slow; others refer to massively parallel approaches. For parallel approaches, we depict the total printing rate. Ideally, the same type of benchmark structure should have been 3D printed for all approaches, which would allow for a direct and fair comparison.

Unfortunately, the field has not yet reached that level of maturity yet. For example, when printing 3D structures with low volume filling fraction by fully parallelized approaches, the effective printing rate would need to be down-corrected with respect to sequential approaches, for which the effective printing rate does not depend on the volume filling fraction. Therefore, we must live with the information at hand. This also means that we depict the peak voxel printing rate, which does not include any kind of settling times or overhead times required to process and transfer digital information from the computer to the machine tool. These overheads can take a substantial fraction of the total printing time though.^[5] Again, such information is not consistently available for all approaches and, hence, we cannot include it in our overview.

The labels of the data points in Figure 1 correspond to the following references of this paper: 2005,^[6] 2006,^[7] 2007,^[8] 2008,^[9,10] 2011,^[11,12] 2012,^[13–15] 2014,^[16–19] 2015,^[20–23] 2016,^[24,25] 2017,^[2,26] 2018,^[27–29] and 2019.^[30–33]

Let us compare the different approaches shown in Figure 1 and, in passing, briefly explain their operation principle in each case. These are:

- 1) Electron beam induced deposition (EBID, red open squares),
- 2) Selective laser sintering (SLS, dark-red diamonds),
- 3) Electrohydrodynamic (redox) printing (EHDP, light-blue left-pointing triangles)
- 4) Direct ink writing (DIW, light-blue downward-pointing triangles),
- 5) Fused filament fabrication (FFF, blue right-pointing triangles),
- 6) Inkjet 3D printing (IJ, dark-blue upward-pointing triangles),
- 7) Projection microstereolithography (PμSL, light-green discs),
- 8) Continuous liquid interphase printing (CLIP, dark-green circles),
- 9) Computed axial lithography (CAL, yellow stars), and
- 10) Two-photon printing (2PP or, more generally, multiphoton printing, red squares).

In (focused) EBID, an electron beam deposits material from a low-pressure gaseous environment, while raster-scanning over a substrate. A great variety of materials can be deposited, e.g., plastics and metals.^[34] However, there are constraints regarding the possible geometries that can be made. For instance, no lines orthogonal to the electron beam are easily feasible.^[28,35] However, the resolution is conceptually only limited by the molecule's size. Yet, EBID is often not listed among other 3D printing techniques, which is due to its slow printing speed of about 1 voxel s⁻¹ or below.^[9] This technique is conceptually very similar to (focused) ion-beam induced deposition (IBID).

SLS uses a focused laser beam to fuse a powder into a solid material.^[36] A galvanometric motor rapidly scans the laser across a flat surface of powder. Once a layer is fully printed, a layer of fresh powder is applied. The galvanometer mirrors achieve scanning speeds of the focus of a few meters per second. The approach achieves linewidths of about 500 μm which translates to almost 10⁵ voxels s⁻¹. SLS is not limited to plastics, but high laser powers are indispensable.

In EHDP, a sacrificial metal anode, e.g., copper or aluminum, is immersed in a liquid within a printing nozzle.

The solvated metal ions are then deposited onto an electrically (semi)conducting substrate, where they are reduced. By this approach, metallic 3D structures have been printed with speeds up to 10 voxels s⁻¹ and feature sizes of around 250 nm.^[32]

FFF is probably the most widespread 3D printing method to date. A thermoplastic filament is fed into a heated nozzle and is deposited onto a substrate. Either the nozzle or the substrate is scanned in 3D to print the desired structure. While this method is relatively inexpensive and conceptually simple, it is rather slow with printing speeds of only several hundred voxels per second.^[37] Typically, FFF offers a resolution of 500 μm

DIW is similar to FFF in that a nozzle scans over a substrate and continuously deposits material. The main difference is that the material is liquid in DIW. Upon deposition, the “ink” solidifies through different mechanisms, e.g., through coagulation or thermal curing.^[7,18,38,39] As to be expected, the printing speed is similar to that of FFF. The achievable resolution, however, ranges from millimeters to micrometers, depending on the material choice.

IJ is well known and well established from 2D graphical printing, which represents a huge consumer market.^[40,41] Engineers in industry have optimized this approach over many years. State-of-the-art 2D printing speeds are around 10⁷ s⁻¹. IJ is also available commercially for 3D material printing (dark-blue upward-pointing triangles in Figure 1).^[19,26] The basic idea is to extrude liquid material droplets from an array of tiny nozzles, solidify them, and then physically move the print head to the next position. Alternatively, when combined with a powder bed of plastic granulate, the nozzles can be used to dispense small droplets of glue, which are then thermally cured. This approach is the fastest one in Figure 1 with voxel printing rates up to 10⁷ voxels s⁻¹. Ink-jet printing is restricted to voxel sizes between 10 and 100 μm. It should be noted though that, according to communication with the manufacturer, not all architectures can actually be 3D printed. For example, a 3D woodpile crystal^[42] with rods of only one voxel in diameter could not be 3D printed with this technology. Therefore, the effective voxel size is larger than the one quoted and, in principle, the data points in Figure 1 would need to be corrected, such that they would move to the left and downward at the same time. We have not performed this correction. In Figure 1, the number labeled *N* indicates the number of nozzles used in the inkjet printer. For the example of *N* = 15192 in Figure 1, the printing speed for an individual nozzle is below 10³ voxels s⁻¹. Unfortunately, this number is not disclosed for all models.

A series of patents and publications after 1967, including Chuck Hull's patent on stereolithography and earlier ones, mark the genesis of 3D additive manufacturing.^[43–45] In stereolithography, a rasterizing laser cures a liquid monomer. This idea later evolved to PμSL, which is a parallel approach, at least in two of the three dimensions. Here, the two lateral spatial dimensions are defined by projecting a 2D optical image into a plane. In principle, Abbe's diffraction barrier determines the lateral resolution. In practice, the lateral voxel size is much larger than that though, because it is roughly matched to the axial voxel extent. Beer's law, that is the exponential decay of the light intensity in an absorbing medium, determines the extent of the voxel in the third dimension, orthogonal to the plane. Different planes are exposed sequentially. Despite its parallel

nature, P μ SL exhibits among the smallest voxel printing rates, with voxel sizes ranging from ten micrometers to hundreds of micrometers in Figure 1. In the so-called “top-down” approach, the optical image is projected from top into a bath of photoresin.^[14,46] Right underneath the surface, a substrate is used to lower the structure once a layer has been cured. Due to the sample’s drag, one has to wait for some time for the liquid to form a smooth and even layer. In the alternative “bottom-up” approach, the image is projected from below the vat of resin through a transparent window. Here, the printed layers have to be carefully delaminated from the transparent window in order to proceed.

CLIP is closely related to P μ SL, except that the definition of the third dimension is different from P μ SL. In CLIP, 3D printing takes place close to an optically transparent membrane window that is permeable to oxygen.^[23,47] Oxygen quenches the photopolymerization process. Therefore, the to-be-printed object stays disconnected from the membrane window and one hereby avoids the unwanted waiting time present in P μ SL. Another approach is to inhibit polymerization close to the bottom window photochemically.^[48] CLIP tends to be faster than P μ SL in terms of the voxel printing rate, at the prize of yet larger voxel sizes, ranging from hundred micrometers and approaching one millimeter in Figure 1.

When printing large volumes from a photosensitive resist, considerable heat is generated through photochemical processes. A recently introduced 3D printing technique overcomes this problem by placing the photoresist on a bed of inert oil.^[33] The used perfluorinated oil does not mix with the photoresist and is circulated through a chiller to actively cool the photoresist. The exponential intensity decay (Beer’s law) determines the axial extent of the voxel. Using this approach, the authors demonstrated a printing speed larger than 10^5 voxels s^{-1} at a voxel size of 300 μ m. A 0.7 m tall 3D lattice comprising 6480 unit cells was printed within 100 min using this variant of CLIP (their Figure S5). For comparison with our results presented below (using a different, more complex lattice though), 10^5 unit cells would have needed about 26 h of printing time.

CAL is a massively parallel approach in all three dimensions. It is conceptually distinct from both, P μ SL and CLIP. In CAL, a hollow cylindrical tank with optically transparent walls containing a photoresist is exposed by 2D images from many different directions, in the spirit of inverse tomography.^[2,30] The individual illumination pattern have been calculated in advance such that the sum of all exposure doses corresponds to the target 3D object. Only after finishing all exposures, the insufficiently exposed material is removed. This step introduces a certain magic to the process. However, so far, voxel sizes have been in the range 100 μ m to 1 mm and voxel printing rates have been in the range of 10^3 – 10^4 voxels s^{-1} . Both FOM are at the low end in Figure 1, but the technology is young and improvements may be possible. Furthermore, so far, only solid objects have been made along these lines. It remains to be seen whether 3D periodic architectures can be 3D printed, for example, 3D woodpile crystals or complex 3D metamaterial architectures.

As the last approach in this section, we address 2PP, the technology some of the authors of this publication have been using and advancing for many years. Multiphoton printing is a generalization.^[49] 2PP in its original form is a sequential procedure based on scanning one tightly focused laser

beam in three dimensions to “write with a pen of light” in a suitable photoresist material. By means of two-photon (or more generally multiphoton) absorption, the excitation is sufficiently confined in all three dimensions at the same time. After writing a desired pattern, a developer washes out the insufficiently exposed, hence insufficiently crosslinked material. Many groups have obtained sub-micrometer voxel sizes by 2PP, however, at voxel printing rates that scatter over four orders of magnitude in Figure 1. Low rates are usually due to using piezoelectric stages for moving the photoresist, whereas the focus is fixed. High voxel printing rates can be achieved by using motorized galvo-mirrors for moving the focus, while the photoresist itself is fixed. The highest printing speeds have been obtained by using the galvo-mirrors in a resonant mode.^[27] Here, however, the speed of light modulation was a limiting issue so far, leading to enlarged effective voxel sizes with respect to the optical diffraction limit.

Furthermore, the 2PP results in Figure 1 are labeled by N , the number of laser foci scanned in parallel. Naively, the voxel printing rate should be proportional to N . Surprisingly, in sharp contrast, results for $N \gg 1$ tend to be considerably smaller than the ones for just a single focus, $N = 1$. This statement holds true for a publication from 2005 with as many as $N = 227$ foci,^[6] as well as for a 2019 publication with $N = 4$.^[31] This trend is due to the fact that splitting one laser focus into many laser foci is often accompanied by a considerable loss of total power. Unless great care is taken, one can “easily” lose an order of magnitude in power or more. Therefore, the power available in any given focus is insufficient for rapid scanning. After all, the product of scanning speed and the square of the laser power (for two-photon absorption) has to be kept constant to stay at constant exposure dose. Moreover, the galvo-mirror scanning optics has to be built such that it allows for scanning of multiple foci in parallel without obtaining huge focus distortions, which immediately translate into distortions in the to-be-printed 3D structure. Obviously, all optical apertures have to be sufficiently large, too. In addition, the large number of optical components involved in such a setup tends to temporally broaden the laser pulses. This broadening reduces the two-photon absorption efficiency. This reduction can be compensated by larger incident laser power or by appropriate group-velocity dispersion compensation. It goes without saying that 2PP with multiple foci scanned in parallel is restricted to the making of 3D structures containing repetitive 2D patterns. One retains full flexibility in the third dimension (z -direction) though as well as in the xy -plane outside of the laser foci array.

In a fully parallelized 2PP approach, one projects an entire 2D image into a plane at a certain z -position.^[50] Two important aspects should be noted. First, if each 2D pixel of that image containing a million pixels or more should lead to one 3D voxel, the two-photon absorption dose must be kept sufficiently large. This means that the total mean laser power, or the pulse repetition rate, or the exposure time, or combinations thereof need to be adjusted accordingly. Practical realizations went from the typical 100 MHz pulse repetition rate of laser oscillators down by five orders of magnitude to 1 kHz repetition rate of amplified laser systems.^[50] This step is connected to substantially more expensive lasers. The second aspect is yet more fundamental: One must cope with a very much more

pronounced proximity effect. To illustrate this aspect, consider a constant exposure intensity in one z -plane, which one would need, for example, to 3D print a plate. In this case, for weak two-photon absorption, the exposure dose is not only constant in the xy -plane, but also constant as a function of z . This means that one gets a 3D block instead of a 2D plate. Two-photon absorption would have no advantage compared to one-photon absorption. To eliminate this artifact, the concept of temporal focusing has been introduced.^[50] The underlying idea is to illuminate the entrance pupil of the focusing microscope objective lens such that, for each voxel, the different frequency components of the femtosecond laser pulses impinge along the same direction, but are displaced laterally. Thereby, for an ideal lens, the different colors only coincide spatially in the focal region. Thus, one only gets a short laser pulse in the focus at a certain z -position, and longer pulses, hence smaller two-photon absorption rates, at other positions. By virtue of temporal focusing, the pulse length decays linearly away from the focal plane and so does the two-photon absorption dose for the worst case of constant illumination.^[51] For dense illuminations patterns, the situation is similar. This linear axial decay of the exposure dose is dramatically slower than the squared Gaussian decay of a single Gaussian focus of ordinary 2PP. As a result, the doses of two or more nearby planes add up, such that the regions in between are exposed as well. Hence, one does not obtain separated planes at the end of the printing process, but rather a block of material. In other words, more generally speaking, the temporal focusing approach is inherently connected to much more pronounced proximity effects than the single-focus or the dilute multifocus 2PP approach. In a recent paper using temporal focusing, the authors reported a printing rate of 3.33×10^8 voxels s^{-1} . However, they did not demonstrate dense periodic structures along the z -direction, but rather only translationally invariant structures along z and isolated features along z . Both examples are not sensitive to the described proximity effect. We privately contacted the authors immediately after their work appeared and asked them to manufacture the large 3D microstructures we show below, such that a direct comparison between their approach and ours below would be available. They responded that they were unable to perform such benchmarking in the near future. On this basis, we feel that it would be inadequate to include their claims into Figure 1, because their approach is likely not suitable for the making of general complex 3D microstructures, especially if they contain dense periodic features along the z -direction. In Figure 1 we aim to exhibit additive manufacturing approaches that have full 3D printing capability.

Any 2PP, single-focus or multifocus or projection-based, process has to face the fact that the field of view (FOV) with a sufficiently low field curvature of the focusing microscope immersion-lens is finite in the xy -plane. Typical FOV diameters for numerical apertures of $NA = 1.4$ are in the range of $400 \mu\text{m}$. Beyond that scale, different exposures obtained by scanning the sample with respect to the lens have to be stitched together. Obviously, the translation errors of the translation stage should be (much) smaller than the voxel size. In the orthogonal z -direction, the 3D printing strategy must appreciate the fact that the free working distance of the high-NA microscope lens is finite, too. Typical values are few hundred micrometers. Otherwise,

the microscope lens may physically bump into already 3D printed structures.

In what follows, we describe a 2PP machine tool that goes beyond the described state-of-the-art concerning voxel printing rate, yet stays at the state-of-the-art regarding voxel size for 2PP. Thereafter, we apply this improved technology to an example, a 3D mechanical metamaterial composed of an exceptionally large number of unit cells—which would not have been possible without this advance.

3. Rapid Multifocus Two-Photon Printing

A scheme of the 3D printing setup used in our present work is depicted in Figure 2. The setup consists of a femtosecond pulsed Ti:Sa laser (Spectra Physics Mai Tai HP, average power 2.8 W, repetition rate 80 MHz pulse width at laser output 90 fs). For printing the structures, we choose a center wavelength of 790 nm for which the home-built diffractive optical element (see below) is optimized.

An acousto-optic modulator (AOM, AA MT80-A1.5-IR) is used for fast modulation of the beam power, offering a minimal rise time of about 285 ns for 1.2 mm beam diameter. We use typical maximum modulation frequencies at around 1 MHz. For long-time operation, these conditions require cooling of the

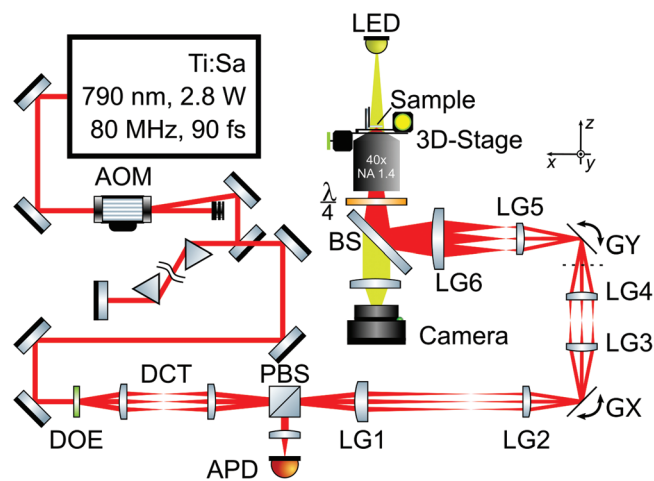


Figure 2. Scheme of the setup used for parallelized 3D two-photon printing. The beam of a Ti:Sa laser (Spectra Physics MaiTai HP) is modulated using an acousto-optic modulator (AOM, AA MT80-A1.5-IR). A prism compressor precompensates for the acquired group delay dispersion. A diffractive optical element (DOE) is placed at the entrance pupil of a dispersion-compensating telescope (DCT). The beam is transmitted through a polarizing beamsplitter cube (PBS). The image of the DOE is demagnified twofold in a second afocal relay (LG1 and LG2) and subsequently imaged onto the galvanometric mirrors (GX and GY) using another relay (LG3 and LG4). The dashed line indicates a flip of the coordinate system. Otherwise, the second galvanometer would point the beam outward the paper plane. In the final relay arrangement (LG5 and LG6), the DOE is imaged through a quarter-wave plate into the objective lens' pupil (Zeiss Plan-Apochromat 40x/NA1.4 Oil DIC) and focused onto the sample. A microscope stage (Märzhäuser-Wetzlar Scan IM 120 × 100) translates sample the in x - and y -directions. A piezoelectric inertia stage (PI Q-545.140) moves the stage along the z -direction. The back-reflected light is focused onto an avalanche photodiode (APD).

driver electronics. The AOM's zeroth diffracted order is guided onto a beam dump.

A prism pulse compressor, consisting of two N-SF10 prisms, precompensates for the $\approx +30\,000\text{ fs}^2$ group delay dispersion which the laser pulses acquire while propagating through the setup.^[52,53] The tip-to-tip distance of the two prisms is 2 m.

The diffractive optical element (DOE) for splitting the beam into $3 \times 3 = 9$ beamlets has been designed by us using an iterative Fourier transform algorithm, as described by Gerchberg and Saxton.^[54] The DOE consists of square pixels with a side length of $2\ \mu\text{m}$, 8 different height levels, and has a total diameter of 6 mm. Due to the diffractive nature of the DOE and due to the finite spectral bandwidth of the femtosecond laser pulses, which is on the order of 10 nm in wavelength, the diffracted beamlets are spatially and temporally stretched. These aspects are taken into account in the design of the DOE by making the diffracted orders intentionally brighter than the zeroth order. The DOE itself has been printed using a Nanoscribe Photonic Professional GT 3D laser printer. An oblique-view scanning electron micrograph of the DOE is shown in **Figure 3**. Due to the Photonic Professional GT's limited FOV, the DOE exhibits stitching artifacts. If the stitching period is an integer multiple of the DOE's period, we have found significant crosstalk between the diffracted orders and the stitching artifact. By deliberately making these two periods incommensurable, we were able to reduce the artifacts drastically. Still, DOEs are notoriously sensitive to fabrication imperfections. Any imperfection deteriorates the power distribution and uniformity among the individual beamlets. Most importantly, the level height of the DOE and hence the accumulated optical path length is generally incorrect after the first iteration of printing due to shrinkage, proximity effects, and field curvature of the writing objective lens. By iteratively printing DOEs and compensating for incorrect step heights, DOEs in which the

individual beamlets all have less than 5% relative power deviation to their design values have successfully been fabricated. The total printing time for the full-size DOE is 50 h (using a scan speed of 10 mm s^{-1} , Nanoscribe's IP-L photoresin and a $63\times/\text{NA}1.4$ objective lens). The DOE's backside has been coated with a single 140 nm thick layer of MgF_2 to suppress reflection losses from the interface between air and the glass substrate.

The DOE is placed at the entrance pupil of a dispersion-compensating telescope (DCT), which is an afocal Keplerian relay with a magnification of nearly unity. This DCT has been described elsewhere and has been provided to us by the respective authors.^[55] The telescope corrects for the aforementioned spatial broadening of the diffracted beamlets by having a strong lateral color, i.e., by having a strong chromatic dependence in the magnification.

A demagnifying telescope (2:1) is placed behind the DCT. It images the DOE onto the first galvanometric mirror. In between the telescopes, we place a polarizing beamsplitter (PBS, Thorlabs PBS252) such that the beam coming from the laser is fully transmitted. The first lens group (LG1) of this afocal relay has been optimized using Zemax (Table S1, Supporting Information), the second lens group (LG2) and the lenses of the following relays (LG3–LG6) have been used and assembled as described previously.^[56] For scanning the fan of beamlets, two galvanometric mirrors (GX and GY, Cambridge Technology 6215H with 6 mm mirror diameter) are used. We operate these at a peak frequency of 2.8 kHz which is just slightly below the frequency of 2.9 kHz at which the electronics cuts off to avoid resonance. To allow for long-term operation of the galvanometric mirrors at such high frequency, we have built and implemented a closed-loop water cooling system.

Behind the tube lens group (LG5 and LG6), a chromatic beamsplitter (BS, AHF 725 DCSPXR) reflects the beams through an achromatic quarter-wave plate (B. Halle Nachfl. GmbH). An objective lens (Zeiss Plan-Apochromat $40\times/\text{NA}1.4$ Oil DIC) focuses the beamlets onto a sample in the fashion of an inverted microscope. The sample is mounted on a piezoelectric stage (PI Q-545.140), which, in turn, is mounted on a microscope precision xy -table (Märzhäuser-Wetzlar Scan IM 120×100). A light emitting diode (LED) installed above the sample and a camera (FLIR Blackfly PGE-50S5M-C) are used to optically monitor the printing process. The quarter-wave plate flips the linear polarization of the back-reflected light such that it is reflected within the PBS. This reflection is focused onto an avalanche photodiode (APD, Thorlabs APD410AM) for focus characterization purposes.

A custom software written by us and running on an FPGA board (NI 7931R and NI 5783) synthesizes the driving signal for the galvanometric mirrors and the AOM and allows for real-time control. Real-time access would be difficult to impossible to obtain by direct control by a personal computer.

4. An Application: 3D Metamaterials

Metamaterials are rationally designed artificial materials exhibiting effective-medium properties that go beyond the properties of their ingredients, qualitatively or quantitatively.^[57] In some cases, the effective properties even go beyond what nature

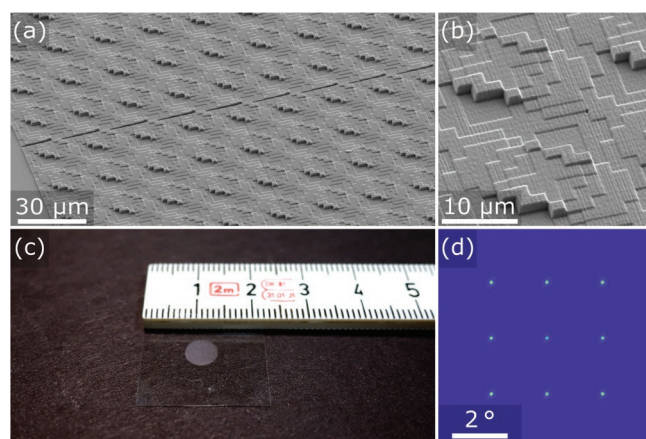


Figure 3. a) Scanning electron micrograph of a 3D printed diffractive optical element (DOE). Such DOE is used in the setup described in Figure 2 to split one incident laser beam into $3 \times 3 = 9$ beamlets. b) Close-up view of the DOE. The pixels have a size of $2 \times 2\ \mu\text{m}^2$ and consist of 8 different height levels. c) Optical photograph of the DOE next to a metric ruler. The substrate is a standard microscope-coverslip with a size of $22 \times 22\text{ mm}^2$. d) Normalized false-color intensity measurement of the DOE using a CMOS-camera. The DOE is illuminated with a 1.2 mm diameter femtosecond pulsed laser beam of 790 nm center wavelength and placed in the back-focal plane of a 50 mm focal length lens.

has to offer. Mechanical metamaterials are an emerging subclass.^[4,58–60] Chiral mechanical metamaterials^[3,61] enable certain linear elastic static and dynamic degrees of freedom that are forbidden on the level of (linear) Cauchy elasticity. For example, when compressing or expanding an ordinary elastic material beam along its axis, a twist of the beam around this axis is not allowed.^[62] Furthermore, when pushing the top of the beam forward, a bending of the beam to the left- or right-hand side is forbidden as well. Clearly, both examples are strictly symmetry-forbidden for an achiral medium. However, for ordinary macroscopic solids, they are “Cauchy-forbidden” even if symmetry allows them to be nonzero. In metamaterial crystals with lattice constants, a , that are much larger than those of ordinary (atomic) crystals, these restrictions do not apply.

Here, we just take the metamaterial architecture introduced in ref. [3] as a complex benchmark example for 3D additive manufacturing. There,^[3] the largest samples had 500 3D unit cells total, which needed a total printing time of about one day for one metamaterial sample, using a commercial 3D laser printer (Nanoscribe Photonic Professional GT).

For convenience of the reader, we repeat the blueprint of the 3D unit cell^[3] in panel (a) of **Figure 4**. Panel (b) shows an optical color photograph of the 3D metamaterial samples which we have 3D printed with the above setup, using $N = 3 \times 3 = 9$ laser foci and a focus speed of 0.4 m s^{-1} . The structure was printed using a hatching distance of 200 nm and a slicing distance of 500 nm. The total printing time (including all settling times, etc.) was about two days. As the photoresist, we have used IP-Dip (Nanoscribe GmbH), while IP-S (Nanoscribe GmbH) has been used in ref. [3]. IP-S would not have been compatible with the objective lens used here. The photoinitiator remaining in the IP-Dip resist gives rise to the yellow color. One of the samples is achiral ($\delta = 0^\circ$), the other one is chiral ($\delta = 34.8^\circ$). Each of the

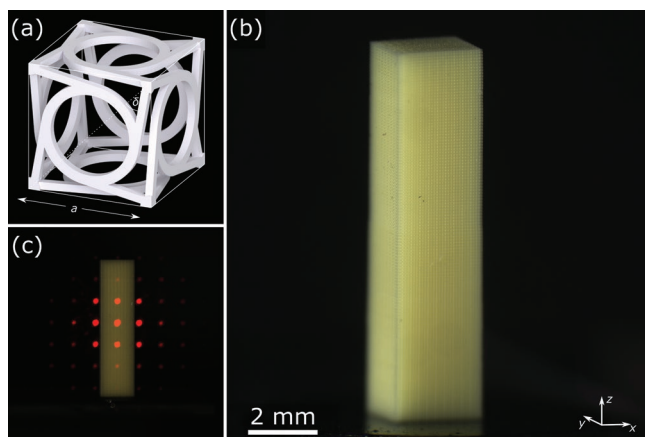


Figure 4. a) Scheme of the chiral 3D metamaterial cubic unit cell with lattice constant a after ref. [48]. b) Photograph of a manufactured chiral metamaterial sample ($\delta = 34.8^\circ$). This sample contains $30 \times 30 \times 120 = 108\,000$ 3D unit cells with $a = 80 \mu\text{m}$ (which is identical to the focus spacing in the laser-focus array), thus a volume of $2.4 \times 2.4 \times 9.6 \text{ mm}^3$. The sample contains about 3×10^{11} voxels printed with a peak printing rate of $0.9 \times 10^7 \text{ voxels s}^{-1}$. c) Laue diffraction pattern of the cubic metamaterial crystal upon exposure with laser light of 633 nm wavelength. This photograph has intentionally been overexposed to reveal the higher diffracted orders. A photograph of the sample has been added for clarity.

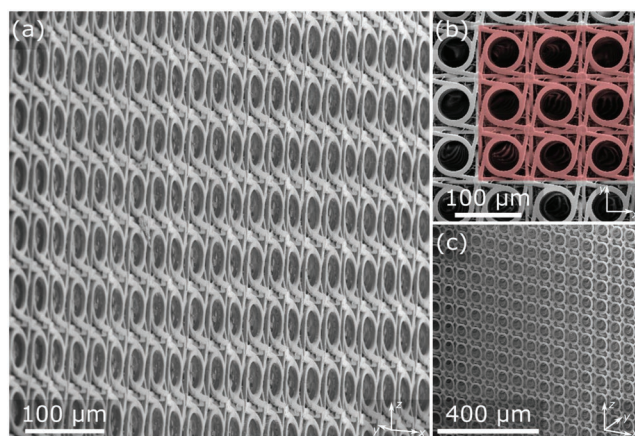


Figure 5. a) Oblique side-view scanning electron micrograph (cf. Figure 4b) of a 3D printed chiral mechanical metamaterial as in Figure 4 with $\delta = 34.8^\circ$. b) Top view exhibiting minor stitching artifacts caused by either the different foci in the 3×3 array and/or the adjacent writing fields. The simultaneously printed 3×3 array is highlighted in red. c) Achiral version of the metamaterial with $\delta = 0^\circ$.

two samples contains a total of $30 \times 30 \times 120 = 108\,000$ 3D unit cells and about 3×10^{11} voxels. We are not aware of any published 3D printed architecture with more voxels than that. While one can hardly resolve the individual metamaterial unit cells on the photograph in Figure 4b or with the bare human eye, the Laue diffraction pattern of the metamaterial taken with a continuous-wave laser at 633 nm wavelength and shown in Figure 4c exhibits sharp peaks—as expected for a 3D crystal. Disorder would lead to broadened Laue peaks and to diffuse scattering of light.

Finally, the electron micrographs shown in panels (a)–(c) in **Figure 5** provides evidence for the high quality of the metamaterial samples. The top view shown in panel (b) illustrates the stitching between the different foci within the 3×3 focus array (which has the same period as the lattice constant a of the metamaterial) as well as the stitching between different adjacent writing fields. The metamaterial structure has become so large that one cannot grasp it in one field of view of our electron microscope (Zeiss SUPRA 55VP).

5. Conclusions

For many applications in optics, mechanics, and biology, one would like to directly convert blueprints, in the form of a digital file on a computer, into 3D hardware, i.e., into materials, devices, and systems. Today, a large variety of different 3D additive manufacturing (a.k.a. 3D printing) approaches allows for doing this by building up matter from small building blocks or “voxels.” The minimum size of the voxel and the maximum voxel printing rate are two decisive FOM. Here, we have reviewed the state-of-the-art of SLS, EHDP, DIW, FFF, IJ, PμSL, CLIP, CAL, 2PP, and EBID in this regard. 2PP approaches perform very well concerning both FOM, despite common prejudice that this serial technique is slow. On the sub-micrometer voxel scale, 2PP, EBID, and certain forms of DIW are presently the only available 3D additive manufacturing options.

Furthermore, we have described and realized a new multifocus 2PP machine tool that approaches total 3D printing speeds of ten million voxels per second at sub-micrometer voxel sizes, significantly surpassing previous best figures of merit. As a first demonstration and application example, we have manufactured microstructured 3D (chiral) mechanical metamaterials comprised of more than one hundred thousand complex 3D unit cells each. This number has to be compared with previous best values in the field of less than one thousand 3D unit cells. We believe that this technological advance will enable future scientific advances in the field of metamaterials, for example, the experimental study of elastic metamaterials with tailored and large characteristic length scales.^[63] Demonstrating such large length scales requires the availability of samples with 10^5 unit cells and beyond. Furthermore, nonprofessionals will immediately accept 3D metamaterials with that many microscale unit cells as shown by the photographs in Figure 4 as “materials” rather than as structures.

In the future, the multifocus multiphoton absorption approach could be extended to laser-foci arrays with yet more laser foci, leading to yet larger peak 3D printing rates. Two aspects will eventually be limiting. First, the overall size of the laser-focus array in the focal plane cannot be increased due to the fundamentally limited field-of-view of the high-NA microscope objective lens. Therefore, more foci mean denser foci spacing. Decreasing the spacing between the foci will become problematic at some point because the electric fields of the foci interfere and substantially distort the exposure pattern, unless measures are implemented to suppress the optical coherence between the foci. Second, for a given photoresist, the required laser power will obviously increase proportionally to the number of laser foci. As the laser power required in our present work was already at around 3 W (out of the laser) for 9 laser foci at 0.4 m s^{-1} scanning speed, working with yet larger powers does not appear to be an attractive avenue. Therefore, developing sensitized photoresist materials with lower polymerization threshold laser powers^[64] that, at the same time, do not deteriorate the sub-micrometer voxel size is very highly desirable.

Supporting Information

Supporting Information is available from the Wiley Online Library or from the author.

Acknowledgements

The authors thank Peter Gumbsch and Patrick Ziemke (both Karlsruhe) for valuable discussions on metamaterials. V.H. thanks Patrick Müller (now Nanoscribe GmbH) and Johann Westhauser (KIT) for hands-on support with the setup. We would like to thank Qinglei Hu and Shaoqun Zeng from Huazhong University of Science and Technology for providing us with the optics for the dispersion-compensating telescope. The authors thank the Institute for Information Processing Technologies (ITIV) at KIT for providing them their Zemax-License. This research was funded by the Deutsche Forschungsgemeinschaft (DFG, German Research Foundation) under Germany's Excellence Strategy via the Excellence Cluster 3D Matter Made to Order (EXC-2082/1-390761711), by the Carl Zeiss Foundation through the “Carl-Zeiss-Focus@HEiKA,”

by the Helmholtz program “Science and Technology of Nanosystems” (STN) and the associated KIT project “Virtual Materials Design” (VIRTMAT), by the Karlsruhe School of Optics & Photonics (KSOP), by the Max Planck School of Photonics (MPSP), and by the KIT Nanostructure Service Laboratory (NSL). C.B.-K. acknowledges the Australian Research Council (ARC) in the context of a Laureate Fellowship enabling his photochemical research program as well as the Queensland University of Technology (QUT) for continued key support. We acknowledge support by the KIT-Publication Fund of the Karlsruhe Institute of Technology. Minor typographical errors were corrected on June 25, 2020 after initial online publication.

Conflict of Interest

The authors declare no conflict of interest.

Keywords

3D additive manufacturing, 3D printing, diffractive optical elements, metamaterials, two-photon lithography

Received: September 20, 2019

Revised: November 14, 2019

Published online: January 22, 2020

- [1] R. L. Truby, J. A. Lewis, *Nature* **2016**, *540*, 371.
- [2] M. Shusteff, A. E. M. Browar, B. E. Kelly, J. Henriksson, T. H. Weisgraber, R. M. Panas, N. X. Fang, C. M. Spadaccini, *Sci. Adv.* **2017**, *3*, eaao5496.
- [3] T. Frenzel, M. Kadic, M. Wegener, *Science* **2017**, *358*, 1072.
- [4] M. Kadic, G. W. Milton, M. van Hecke, M. Wegener, *Nat. Rev. Phys.* **2019**, *1*, 198.
- [5] L. Jonušauskas, D. Gailevičius, S. Rekštytė, T. Baldacchini, S. Juodkazis, M. Malinauskas, *Opt. Express* **2019**, *27*, 15205.
- [6] J. Kato, N. Takeyasu, Y. Adachi, H.-B. Sun, S. Kawata, *Appl. Phys. Lett.* **2005**, *86*, 044102.
- [7] G. M. Gratson, F. García-Santamaría, V. Lousse, M. Xu, S. Fan, J. A. Lewis, P. V. Braun, *Adv. Mater.* **2006**, *18*, 461.
- [8] X.-Z. Dong, Z.-S. Zhao, X.-M. Duan, *Appl. Phys. Lett.* **2007**, *91*, 124103.
- [9] H. Plank, C. Gspan, M. Dienstleder, G. Kothleitner, F. Hofer, *Nanotechnology* **2008**, *19*, 485302.
- [10] Stratasys Fortus 360MC, release **2008**.
- [11] J. Fischer, M. Wegener, *Opt. Mater. Express* **2011**, *1*, 614.
- [12] S. D. Gittard, A. Nguyen, K. Obata, A. Koroleva, R. J. Narayan, B. N. Chichkov, *Biomed. Opt. Express* **2011**, *2*, 3167.
- [13] Stratasys Mojo, release **2012**.
- [14] X. Zheng, J. Deotte, M. P. Alonso, G. R. Farquar, T. H. Weisgraber, S. Gemberling, H. Lee, N. Fang, C. M. Spadaccini, *Rev. Sci. Instrum.* **2012**, *83*, 125001.
- [15] 3D Systems Projet 7000 HD, vendor information, release **2012**.
- [16] Nanoscribe Professional GT, release **2014**.
- [17] T. Bückmann, M. Thiel, M. Kadic, R. Schittny, M. Wegener, *Nat. Commun.* **2014**, *5*, 4130.
- [18] E. B. Duoss, T. H. Weisgraber, K. Hearon, C. Zhu, W. Small, T. R. Metz, J. J. Vericella, H. D. Barth, J. D. Kuntz, R. S. Maxwell, C. M. Spadaccini, T. S. Wilson, *Adv. Funct. Mater.* **2014**, *24*, 4905.
- [19] Stratasys Objet 5000 Connex1, release **2014**.
- [20] L. Yang, A. El-Tamer, U. Hinze, J. Li, Y. Hu, W. Huang, J. Chu, B. N. Chichkov, *Opt. Lasers Eng.* **2015**, *70*, 26.
- [21] W. Yan, B. P. Cumming, M. Gu, *J. Opt.* **2015**, *17*, 075803.

- [22] Ultimaker 2 Extended, release **2015**.
- [23] J. R. Tumbleston, D. Shirvanyants, N. Ermoshkin, R. Januszewicz, A. R. Johnson, D. Kelly, K. Chen, R. Pinschmidt, J. P. Rolland, A. Ermoshkin, E. T. Samulski, J. M. DeSimone, *Science* **2015**, 347, 1349.
- [24] EOS P 770 with PA 2200 Top Speed 1.0, datasheet and vendor information, release **2016**.
- [25] EOS FORMIGA P 110 with PA 2200 Top Quality 1.0, datasheet and vendor information, release **2016**.
- [26] HP JetFusion 3D 4210, release **2017**.
- [27] B. W. Pearre, C. Michas, J.-M. Tsang, T. J. Gardner, T. M. Otchy, *Addit. Manuf.* **2019**, 30, 100887.
- [28] L. Keller, M. Huth, *Beilstein J. Nanotechnol.* **2018**, 9, 2581.
- [29] W. Chu, Y. Tan, P. Wang, J. Xu, W. Li, J. Qi, Y. Cheng, *Adv. Mater. Technol.* **2018**, 3, 1700396.
- [30] B. E. Kelly, I. Bhattacharya, H. Heidari, M. Shusteff, C. M. Spadaccini, H. K. Taylor, *Science* **2019**, 363, 1075.
- [31] Q. Geng, D. Wang, P. Chen, S.-C. Chen, *Nat. Commun.* **2019**, 10, 2179.
- [32] A. Reiser, M. Lindén, P. Rohner, A. Marchand, H. Galinski, A. S. Sologubenko, J. M. Wheeler, R. Zenobi, D. Poulikakos, R. Spolenak, *Nat. Commun.* **2019**, 10, 1853.
- [33] D. A. Walker, J. L. Hedrick, C. A. Mirkin, *Science* **2019**, 366, 360.
- [34] I. Utke, P. Hoffmann, J. Melngailis, *J. Vac. Sci. Technol., B: Microelectron. Nanometer Struct.* **2008**, 26, 1197.
- [35] L. Hirt, A. Reiser, R. Spolenak, T. Zambelli, *Adv. Mater.* **2017**, 29, 1604211.
- [36] J. J. Beaman, C. R. Deckard, US4938816A, **1990**.
- [37] J. Go, S. N. Schiffres, A. G. Stevens, A. J. Hart, *Addit. Manuf.* **2017**, 16, 1.
- [38] G. M. Gratson, M. Xu, J. A. Lewis, *Nature* **2004**, 428, 386.
- [39] E. B. Duoss, M. Twardowski, J. A. Lewis, *Adv. Mater.* **2007**, 19, 3485.
- [40] E. M. Sachs, J. S. Haggerty, M. J. Cima, P. A. Williams, US5204055A **1993**.
- [41] B.-J. de Gans, P. C. Duineveld, U. S. Schubert, *Adv. Mater.* **2004**, 16, 203.
- [42] K. M. Ho, C. T. Chan, C. M. Soukoulis, R. Biswas, M. Sigalas, *Solid State Commun.* **1994**, 89, 413.
- [43] W. K. Swinson, DE1797599 (A1), **1974**.
- [44] H. Kodama, *Rev. Sci. Instrum.* **1981**, 52, 1770.
- [45] C. W. Hull, US4575330 A, **1986**.
- [46] X. Zheng, H. Lee, T. H. Weisgraber, M. Shusteff, J. DeOtte, E. B. Duoss, J. D. Kuntz, M. M. Biener, Q. Ge, J. A. Jackson, S. O. Kucheyev, N. X. Fang, C. M. Spadaccini, *Science* **2014**, 344, 1373.
- [47] R. Januszewicz, J. R. Tumbleston, A. L. Quintanilla, S. J. Mecham, J. M. DeSimone, *Proc. Natl. Acad. Sci. USA* **2016**, 113, 11703.
- [48] M. P. de Beer, H. L. van der Laan, M. A. Cole, R. J. Whelan, M. A. Burns, T. F. Scott, *Sci. Adv.* **2019**, 5, eaau8723.
- [49] T. Baldacchini, *Three-Dimensional Microfabrication Using Two-Photon Polymerization*, Elsevier, Amsterdam **2016**.
- [50] S. K. Saha, D. Wang, V. H. Nguyen, Y. Chang, J. S. Oakdale, S.-C. Chen, *Science* **2019**, 366, 105.
- [51] G. Zhu, J. van Howe, M. Durst, W. Zipfel, C. Xu, *Opt. Express* **2005**, 13, 2153.
- [52] W. Dietel, J. J. Fontaine, J.-C. Diels, *Opt. Lett.* **1983**, 8, 4.
- [53] R. L. Fork, O. E. Martinez, J. P. Gordon, *Opt. Lett.* **1984**, 9, 150.
- [54] R. W. Gerchberg, W. O. Saxton, *Optik* **1972**, 35.
- [55] Q. Hu, Z. Zhou, X. Lv, S. Zeng, *Opt. Lett.* **2016**, 41, 207.
- [56] J. N. Stirman, I. T. Smith, M. W. Kudenov, S. L. Smith, *Nat. Biotechnol.* **2016**, 34, 857.
- [57] R. S. Kshetrimayum, *IEEE Potentials* **2005**, 23, 44.
- [58] K. Bertoldi, V. Vitelli, J. Christensen, M. van Hecke, *Nat. Rev. Mater.* **2017**, 2, 17066.
- [59] J. Bauer, L. R. Meza, T. A. Schaedler, R. Schwaiger, X. Zheng, L. Valdevit, *Adv. Mater.* **2017**, 29, 1701850.
- [60] J. U. Surjadi, L. Gao, H. Du, X. Li, X. Xiong, N. X. Fang, Y. Lu, *Adv. Eng. Mater.* **2019**, 21, 1800864.
- [61] J. I. Lipton, R. MacCurdy, Z. Manchester, L. Chin, D. Cellucci, D. Rus, *Science* **2018**, 360, 632.
- [62] R. S. Lakes, R. L. Benedict, *Int. J. Eng. Sci.* **1982**, 20, 1161.
- [63] P. Ziemke, T. Frenzel, M. Wegener, P. Gumbsch, *Extreme Mech. Lett.* **2019**, 32, 100553.
- [64] Z. Li, N. Pucher, K. Cicha, J. Torgersen, S. C. Ligon, A. Ajami, W. Husinsky, A. Rosspeintner, E. Vauthey, S. Naumov, T. Scherzer, J. Stampfl, R. Liska, *Macromolecules* **2013**, 46, 352.